Intrinsic dust transport in ASDEX upgrade studied by fast imaging

F. Brochard[a,*], V. Rohde[b], T. Lunt[b], G. Suárez López[b], A. Shalpegin[a], R. Neu[b,c], ASDEX Upgrade Team

[a] *Institut Jean Lamour, Université de Lorraine, UMR 7198 CNRS, 54011 Nancy cedex, France*
[b] *Max Planck Institut für Plasmaphysik, Boltzmannstrasse 2, 85748 Garching, Germany*
[c] *Technical University of Munich, Boltzmannstrasse 15, 85748 Garching, Germany*

A B S T R A C T

Fast video data recorded from 2008 to 2012 in full-tungsten ASDEX Upgrade have been analyzed with the TRACE algorithm developed to automatically detect and track dust particles. The purpose of the work presented in this paper is to complete earlier study of the influence of various discharge conditions on dust rates with an investigation of dust motion under most remarkable conditions. The 3D trajectories of intrinsic dust particles have been confronted to simulations carried out with the DUCAD (Dust Characterization And Dynamics) code, based on the Orbital Motion Limited (OML) approach for dust/plasma interaction modelling. The motion of micrometric spherical dust grains is found to be largely dominated by inertia in the considered experimental conditions. The influence of Vertical Displacement Events (VDEs) and of various heating scenarios on dust areas of formation and trajectories is investigated. It is found that VDEs inject dust originating from the PFCs which are heated by contact with the plasma, upward VDEs having a stronger impact on dust rates and transport than downward VDEs. The use of Neutral Beam Injection (NBI) significantly enhances dust production and transport coming from sectors where injectors are installed. On the contrary, Ion Cyclotron Resonance Heating significantly reduces dust rates and transport in the whole plasma volume.

1. Introduction

Dust generated at the wall of fusion devices may cause operational and safety issues in next generation fusion devices such as ITER [1]. For these reasons, dust generation, remobilization and transport in fusion devices have motivated many studies worldwide since more than a decade [2–13]. In situ observations of intrinsic dust mainly rely on the use of imaging diagnostics which provide rather detailed measurements of dust motion. Such video data provide valuable insight on dust dynamics and confirm the dominant role in dust motion of the ion drag force, but remain insufficient for validating dust transport models due to uncertainties in dust characteristics such as size, morphology, or temperature. Even in controlled injection experiments the modelling of metallic dust, whose motion is dominated by inertia [12,13], is subject to significant uncertainties in regard to initial conditions such as dust size and velocity [14]. The use of fast imaging is however not only devoted to benchmark dust transport codes. Recently, we have used fast imaging to carry out a statistical survey of the influence of various discharge parameters on dust rates in ASDEX Upgrade (AUG) [15]. In the present contribution, we make use of the yet unexploited spatial and temporal information in order to investigate open questions raised by this previous investigation. The main purpose of this contribution is to better identify how plasma conditions and heating scenario influence dust formation areas and transport. After introducing the experimental analysis techniques used to carry out our study and the DUCAD code used for modelling [16], we present the main results derived from the analysis of intrinsic dust 3D trajectories. Then we present our observations on the influence on dust spatial distribution and trajectories of vertical displacement events (VDE) and heating scenarios based on Neutral Beam Injection (NBI), before conducting a more detailed investigation on the influence of the use of Ion Cyclotron Resonance Heating (ICRH). Finally, main results and prospects are summarized in the conclusion.

2. Experimental techniques

The experimental results presented in this contribution are based on the analysis of 2425 discharges recorded on ASDEX Upgrade in between 2008 and 2012 (i.e. discharges 23174 to 28695). Video data recorded by up to 3 fast cameras (Phantom v7.1, Phantom v7.3 and Photron
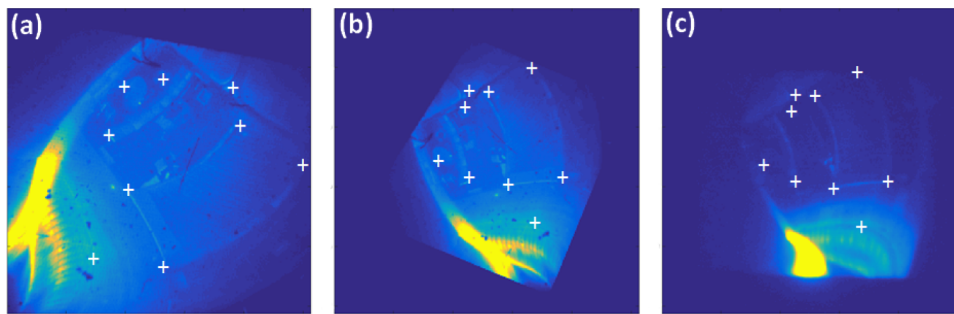
Fig. 1. Illustration of the spatial recalibration after camera re-installation in the same sector but with different optics. (a) Reference camera frame recorded in shot 27460 (false colors), with 9 reference points indicated by white crosses. (b) The same frame after geometrical transformations performed to match the target camera picture recorded in shot 26026 (c). (color online).

SA1.1) have been analyzed automatically with the TRACE code, according to the procedure presented in [15].

Single fast camera measurements have been mostly used to evaluate dust rates under various discharge conditions in [15]. In the present contribution, these measurements are also used to assess dust formation or remobilization areas and to estimate the direction of their motion. For a given camera position, lines of sight (LOS) may vary significantly due to the use of different lenses or different optical setups. The camera locations have been changed up to 8 times in the frame of individual experimental campaigns and LOS are never exactly identical after re-installation at a given location. On addition, mobile parts of the optical setup are subject to vessel vibrations, which result in LOS being shifted after some shots. As a consequence, it is mandatory to check and recalibrate all the camera views before any accurate spatial analysis becomes possible. The procedure, illustrated in Fig. 1, is based on the identification of reference point's pairs easily recognizable in several sets of videos. Geometric transformations are applied to the image which needs to be recalibrated until the position of all the reference points coincide with their positions in the target image. In order to ensure good accuracy, lines of sights have been recalibrated on average every 50 shots. Recalibration procedure is more difficult after the replacement of Plasma Facing Components (PFCs), which may cause the disappearance of several reference points, as for instance after the installation of RMP coils after shot 25945. In the end, in order to recalibrate 2008 and 2012 views, up to 11 iterations with intermediate views have been realized. Finally, recalibration is sometimes not possible for sets of tens of videos because PFCs are not sufficiently visible to identify point pairs. The corresponding data are therefore not taken into account in our analysis.

In addition to single camera measurements, two series of stereoscopic camera measurements were also carried out, in 2010 (shots 26023–26067) and 2012 (shots 28581 – 28695). The aim of stereoscopic measurements was to reconstruct dust motion in 3D and to compare experimental trajectories with dedicated modelling, in order to infer some dust particle's properties such as their sizes. For that purpose, LOS for each camera were determined by adjusting fast camera images to CAD drawings of the vessel by using the AUGDDD software [17]. Taking as a basis the 2D trajectories provided by TRACE for the first camera, dust trajectories in 3D were obtained by computing intersections with the LOS corresponding to the same trajectories observed with the second camera, following the procedure presented in [12]. Practically, LOS never intersects exactly and triangulation is performed. The accuracy in dust position is of the order of a few centimeters and goes inversely with the distance along the LOS.

3. DUCAD transport code

Modelling of 3D dust trajectories has been carried out with the DUCAD (Dust Characterization And Dynamics) code [16], inspired by DUSTT [2], DTOKS [5] and MIGRAINe [10] codes, in an attempt to retrieve dust size from the comparison between simulated and experimental trajectories. DUCAD integrates the Orbital Motion Limited

(OML) [18] approach for modelling dust/plasma interactions: in order to calculate currents to the dust grain, the latter is considered as a perfectly spherical probe embedded in plasma. Hence, collection of electrons and ions by the grain are described as an orbital problem. DUCAD focuses on four different observables: dust charge number, temperature, mass evolution and dynamics by solving the corresponding differential equations.

Dust charging is described by the differential equation:

$$dQ_d/dt = \sum I_i + I_e + I_{th} + I_{see}$$

where $Q_d = Ze$ is the dust grain charge, I_i and I_e the ion and electron currents to the grain, I_{th} is the thermionic emission from the grain and I_{see} the secondary electron emission. In usual SOL conditions, dust charging time is typically 10^3 times faster than the residence time of the dust grain in one of the cells of the computational grid [16,19]. Dust charging can therefore be considered as an instantaneous process and the local charge value can be used, meaning $I_{tot} = \Sigma I_i + I_e + I_{th} + I_{see} = 0$. For the calculation of ion current, a shifted Maxwellian distribution, due to the relative velocity between the grain and the ion flow is considered [1] while the electron current is calculated according to [18]. Thermionic emission is calculated following the Richardson and Dushman work for negatively charged dust corrected for taking into account the Shottky effect [10,20]. I_{see} is calculated by integrating the electron velocity distribution along with the SEE cross section, the energy yield being computed using the Young-Dekker formula [21]. Practically, I_{tot} is calculated for a whole range of possible charge numbers Z. The chosen charge number Z is obtained at the minimum of $|Itot|$, for which $I_{tot} \sim 0$.

For dust heating, the following differential equation for the molar enthalpy of the dust is solved:

$$d(M_d h_d)/dt = \sum Q_i + Q_e + Q_{th} + Q_{see} + Q_{isn} + Q_{rad} + Q_{vap}$$

where h_d is the specific enthalpy, Q_i and Q_e are the heat flux due to collected ions and electrons respectively [1], Q_{th} is the heat flux associated with thermionic emission [10], Q_{see} is the heat flux due to secondary electron emission [10], Q_{isn} is the heat flux due to ion surface neutralization [10], Q_{rad} accounts for the thermal emissivity losses [22,23] and Q_{vap} is the heat flux due to vaporized atoms [10].

The only mass variation mechanism included in DUCAD is the mass loss due to vaporization, calculated using the Hertz-Knudsen formula [24].

Finally, DUCAD solves the equation of motion $M_d \, dV_d/dt = \Sigma F_d$ by including forces due to collection and scattering of plasma ions amongst which the ion drag force dominates [1], electrical forces, gravitational force, neutral friction force [1] and rocket force [8]. DUCAD includes a really simple scheme based on restrictive assumptions in order to implement the rocket force without the computational cost of a more sophisticated method: n being the time step, the heat balance $dH/dt = P_{Heat} - P_{Loss}$ is used to derive the dust temperature T^+_n which is attributed only to the exposed half of the sphere, the one in direct contact with the plasma stream. The temperature of the shadowed half
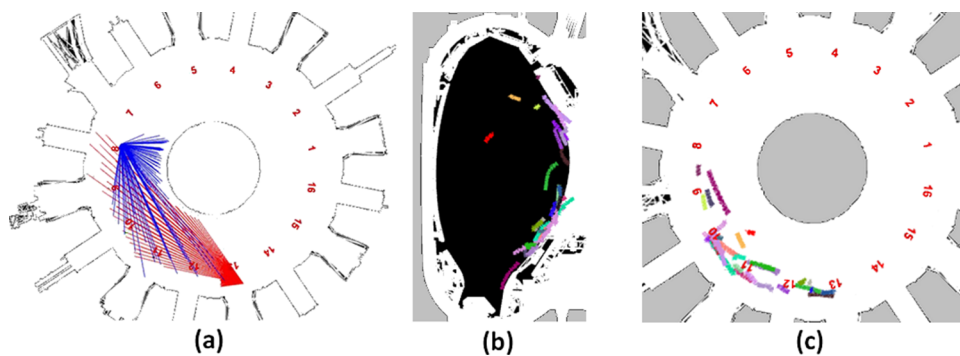
Fig. 2. Top view of the AUG vessel showing the LOS of the Photron SA1.1 camera, in blue, and LOS of the Phantom V7.1, in red, in stereoscopic measurements (a). Poloidal view (b) and top view (c) of the reconstructed dust trajectories. All the trajectories remain in the SOL (the trajectory depicted in red is observed at the very end of the ramp-down phase). (color online).

of the sphere T^{-}_{n} is obtained by assuming that the heat conductivity along the dust grain yields $T^{-}_{n+1} = T^{+}_{n}$, which is a good approximation as long as the time step is kept reasonably small. A more realistic determination of T^{-} should be based on a diffusion law. In the simulations presented in this paper the time step was set equal to 50 microseconds, i.e. small enough to provide stable results while keeping the computation time reasonable. This procedure differs from the one used in [8] where it is considered that the exposed surface is in thermal equilibrium with the impinging plasma heat flux. Strictly speaking, it is shown in [16] that the effective time for achieving thermal equilibrium is of the order of some milliseconds meaning that dust grains with velocities 10 – 100 m/s hardly approach thermal equilibrium before migrating to a different part of the reactor vessel with different plasma parameters and hence, different equilibrium temperature. More details on the calculation and implementation of forces in the DUCAD code, as well as the code itself are provided in reference [16].

Plasma parameters are taken from simulations with the transport code EMC3-EIRENE to which DUCAD has been coupled. The results presented in this contribution are based on EMC3-EIRENE simulation of shot n°29464, with a computational grid extended to the wall. Finally, dust particles are considered as pure tungsten spheres, whose initial position and velocity injected in DUCAD are determined according to experimental observations.

4. Results and discussion

As pointed out in [15], dust rates deduced from fast video measurements are significantly lower in full-W ASDEX Upgrade than in tokamaks with carbon PFCs, with an average rate of 1.35 dust particle per second, while 52% of the shots appear as free of visible moving dust. In reference [15], disruptive shots, which exhibit the largest dust rates, were investigated separately from non-disruptive shots. In the present paper, both disruptive and non-disruptive shots are included in the same data set in order to improve statistics on dust origin and direction, but only dust trajectories detected at least 0.1 s before disruption are kept in order to ensure that they are not caused by disruption. Stereoscopic camera measurements were originally conducted with the aim to investigate intrinsic dust motion under various discharge conditions. However, due to the low dust rates in AUG, 3D trajectories reconstruction turned out to be possible for only 34 dust particles mostly observed in similar discharge conditions, leaving the determination of dust size as the main objective of DUCAD simulations. In the first part of this section, we present the main characteristics of the obtained trajectories and report on the main conclusions drawn from the comparison with modelled trajectories for different dust grain sizes. In the second part of this section, we present a spatial investigation of dust origin and motion in 2D based on single camera measurements. The much better statistics made it possible to identify interesting features under given discharge conditions. Here, we detail the main observations realized during VDEs and during the operation of the different auxiliary heating systems.

4.1. 3D dust motion

For stereoscopic measurements, two monochromatic fast cameras were installed in sector 8 and 13 of AUG as shown in Fig. 2(a). Both cameras were synchronized and recorded videos at 10,000 frames per second. The overlapping volume between the lines of sight of both cameras was approximately 2 m³. The 34 trajectories reconstructed by TRACE 3D are presented in Fig. 2(b) and 2 (c). Comparison with magnetic field lines shows that dust particles move in the SOL, a few ones disappearing after approaching the separatrix. Dust motion is roughly oriented along the magnetic field lines, both in clock- and counter-clockwise directions. The average dust speed is 77 m/s with a standard deviation of 28 m/s. The average dust observation time is 7.1 ms and the total lengths of trajectories vary from 0.3 m to 1.3 m.

In order to infer dust size, DUCAD simulations have been done with the aim to reproduce selected experimental trajectories. The homogeneous parts of the trajectories are ordinary well reproduced, particularly in the toroidal direction, but only little influence of dust size is observed. It appears that due to the large initial velocity (in the range from 30 m/s to 100 m/s), the particle size required for the plasma forces to alter the trajectories dictated by inertia within the observation time is actually much smaller than that measurable with fast camera techniques (e.g. the modelling of 0.1 μm dust shows a clear effect of plasma forces even with large initial velocities, but such small particles cannot be seen with fast cameras [15]). In particular, in all the reconstructed trajectories, the displacement in the clock- or counter-clockwise direction is not dictated by plasma forces but by the large initial velocity. The only case where a sudden change in particle direction is observed is due to the collision of a dust grain with the limiter of an ICR antenna (cf. Fig. 3). Such collisions at the wall are unavoidable and illustrate the importance of dust-PFC mechanical impacts in dust migration around the torus, as also reported in [9,25].

The main visible effect of varying dust size in simulations is to modify dust lifetime, smaller dust being ablated faster than larger dust. Such a case is illustrated in Fig. 4 where the smallest dust grain gets ablated before it completes half of the trajectory, as it approaches close to the separatrix. In this case, the detailed examination of the simulation presented in [16] shows that as dust temperature increases, dust acceleration is mostly due to the rocket force which dominates the ion drag force by more than one order of magnitude. Since the post-mortem analysis of dust collected in AUG in a period close to our observations shows a wide variety of compositions and morphologies [26], it is very likely that the discrepancies between the experimental and modelled trajectories with respect to the poloidal plane are caused by non-uniform rocket force arising from a non-spherical/multi-material particle, whereas our model is based on the assumption of spherical homogeneous tungsten particles.

In the end, it is possible to conclude that stereoscopic observations of dust motion bring little information on the validity of the dust dynamics models for heavy metallic dust, whose motion is dominated by inertia, as also reported in [12,13]. The measured lifetime of glowing
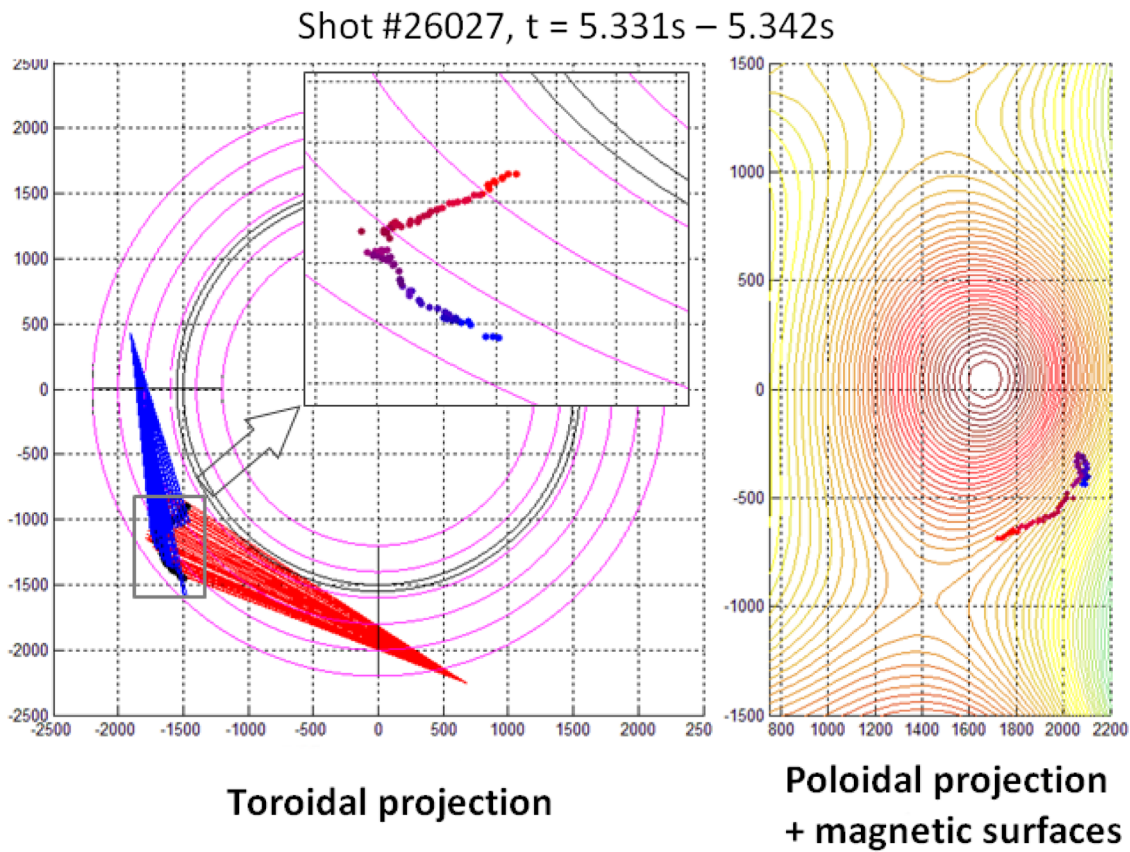
Shot #26027, t = 5.331s − 5.342s

Toroidal projection

Poloidal projection + magnetic surfaces

Fig. 3. (a) Toroidal projection and (b) poloidal projection of the trajectory of a dust particle experiencing a collision with the ICR antenna limiter. First steps of the trajectory are depicted in blue and final steps in red (color online).
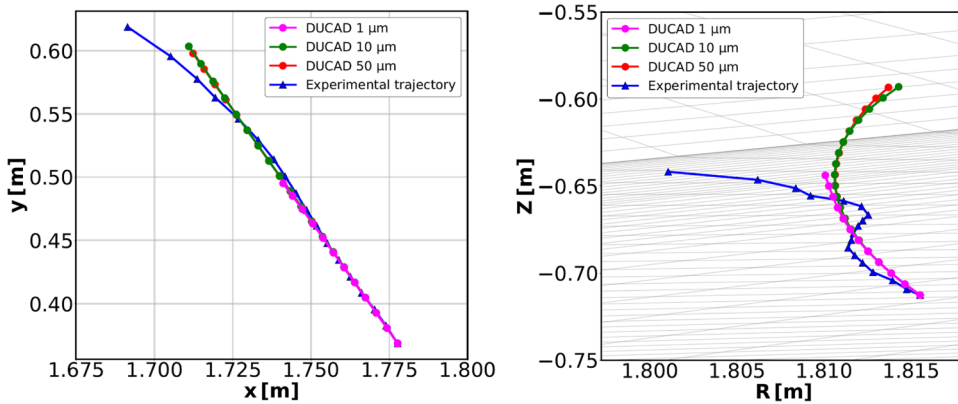

Fig. 4. Comparison between an experimental dust trajectory (solid blue line) and simulated trajectories for tungsten dust grains of three different radii: 1 μm (magenta), 10 μm (green) and 50 μm (red). Left picture shows projections of the trajectories in the toroidal view and right picture in the poloidal view. Markers show the dust positions at regular time interval, highlighting its acceleration in the last part of the trajectory (color online).

particles is the main source of information for estimating dust size, as far as the heat balance model can be trusted. In our study, the best fit between DUCAD simulations and AUG experimental trajectories leads to an initial radius of dust particles of roughly 10–50 μm. This estimated range does not take into account the possible errors on the three-dimensional position of the observed dust particles. The plasma parameters modifications resulting from these errors and the possibility for other dust compositions and morphologies might significantly expand this range. In addition, it has to be noted that OML-based simulations are known to underestimate dust lifetimes in fusion environments [6,7,12,13] and improvements of the heat balance models are currently the object of intense research, as reported in [14]. Finally, this analysis remains inconclusive regarding the nature of the observed dust, i.e. whether it is remobilized or freshly generated.

4.2. Dust in VDEs

Earlier investigation of dust rates in disruptions with VDEs demonstrated significant differences between upward and downward displacements, upward VDEs causing rates larger by a factor of about 2 [15]. This discrepancy was assumed to be due to a faster cooling of the plasma in the case of downward VDEs. The spatial distribution of dust events and trajectory characteristics during VDEs further supports this explanation. Dust trajectories observed in the time interval going between 0.1 s before disruption and the end of the video are depicted in Fig. 5(b) for 13 upward VDEs and in Fig. 5(c) for 30 downward VDEs. Fig. 5(a) represents the reference view from sector 13 to 8 which is also used in the rest of the paper.

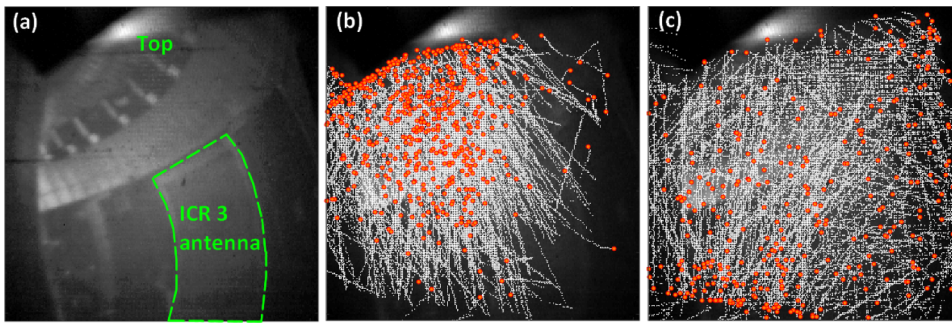Despite the number of upward VDEs considered is much less, more

Fig. 5. (a) Reference view used for recalibration of dust trajectories observed with the camera viewing AUG sector 8 from sector 13 (mirror view). (b) Dust trajectories reconstructed during 13 disruptions with upward VDEs. (c) Dust trajectories reconstructed during 30 disruptions with downward VDEs. Red spots depict the initial point of each trajectory (color online).

dust trajectories are observed, i.e. 634 in upward VDE versus 387 in the case of downward VDEs. Of course, this camera view better shows the upper part of the vessel, which might suggest that not all the dust remobilized from the lowest part of the vessel intersect the camera LOS. This is certainly partly true, but it has to be remembered that data collected in other camera views, imaging also the lowest part of the vessel such as depicted in Fig. 1 have been recalibrated and included in Fig. 4. Also, it is interesting to note that trajectories reconstructed during downward VDEs show a larger variation: 66.7% of the dust particles tracked during downward VDEs move upwards, whereas 97% of the particles tracked during upward VDEs move downward. The projection of the dust trajectories on the vertical plane yields an average velocity of 80.7 m/s for dust in upward VDEs and 40.4 m/s in downward VDEs, while the acceleration is close to zero in both cases. These results are consistent with a much larger energy release to the wall during upward VDEs than during downward VDEs, resulting in larger dust rates and particles ejected with 2 times larger speed.

4.3. Influence of heating scenario

4.3.1. NBI and ECRH

Heating scenarios based on the use of ECRH or NBI are those which lead to the largest dust rates observed by fast cameras in AUG, as shown in Table 1. The spatial investigation of dust events in discharges with or without ECRH confirms this trend, but the higher dust rates observed with ECRH are not obviously correlated to any privileged dust formation area. This denotes that ECRH has a global effect on dust production and remobilization in the whole vessel. There is no particular feature in dust trajectories, which are very similar w/wo ECRH.

The situation is very different when considering the influence of NBI. Fig. 6(a) depicts dust trajectories reconstructed in discharges where NBI was the only auxiliary heating source. 565 dust trajectories have been reconstructed corresponding to cumulated plasma duration of 583 seconds. This picture shows a significant fraction of dust originating from sector 7, hidden by the inner wall on the left of the picture. More precisely, 70.5% of dust particles are moving to the right, the mean dust displacement to the right being 18.4 pixels. These observations significantly differ from those realized in the absence of NBI, as depicted in Fig. 6(b). When no NBI is used (i.e. in discharges with ECRH and/or ICRH), 221 dust trajectories have been reconstructed for a total plasma duration of 1660s. In this case, despite the toroidal field was not reversed, it is striking that 65% of the dust particles move to the left (i.e. towards sector 7), their mean displacement being 8.8 pixels in this direction. The mean vertical displacement is nearly the same with NBI (1 pixel upwards) and without NBI (1.8 pixel upwards), hence only the
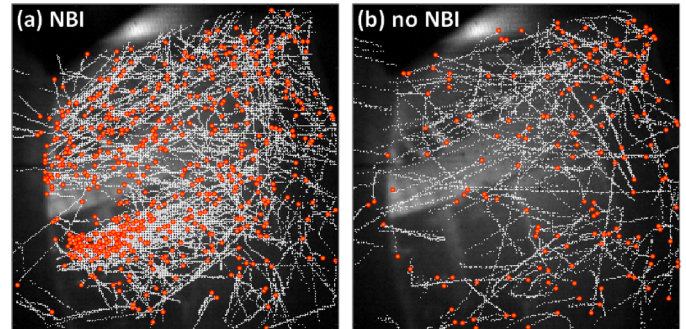

Fig. 6. (a) Dust trajectories reconstructed in 583 seconds of discharge with NBI as the only auxiliary heating system. Dust particles mostly move to the right. (b) Dust trajectories reconstructed during 1660 seconds of discharges without NBI. Dust particles mostly move to the left, i.e. towards sector 7. (color online).

toroidal motion is affected by NBI. The investigation of camera data recorded in sector 1 leads to similar observations, with more dust particle originating from sector 15 in shots with NBI while the tendency is opposite in discharges without NBI.

Despite there are no fast camera data with views directed towards sectors 7 and 15, where the NBI systems are installed, the large dust rates observed in adjacent sectors during NBI operation can only be explained, given the short dust lifetime, by the increased dust production localized nearby the operating NBI. Regarding the direction of dust motion, it is not possible to conclude whether NBI induces toroidally reverse motion in the whole plasma volume or if dust simply escapes symmetrically from sectors where NBI systems are installed. Indeed, almost all the camera measurements available correspond to FOV centered on sector 8 and 1, i.e. upstream with respect to sectors with NBI are installed. The rare measurements directed downstream with respect to NBI are not statistically meaningful given the low dust rate in AUG.

4.3.2. Influence of ICRH

In our previous investigation, it was found that the lowest dust rates are observed when ICRH is used, alone or in combination with other heating sources [15] (see also Table 1). This result was rather unexpected since the erosion of antenna limiters resulting from their interaction with the SOL is known to increase the impurity production. For instance, in the same period of reference as the one covered by our study, the antenna limiters, coated with tungsten, have been shown to account for about two thirds of the W content in the plasma [27]. Despite the impurity release is expected to be essentially due to sputtering,

Table 1

Dust rates per second per MW of heating power for various combinations of heating scenarios. After [15].

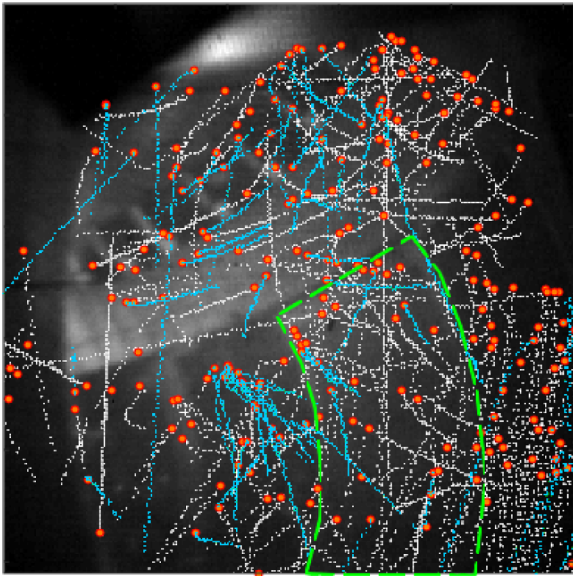|	ECRH	NBI	ICRH	ECRH + NBI	ICRH + NBI	ECRH + ICRH	ECRH + NBI + ICRH
# shots	94	151	15	92	92	8	93
Dust rate /s/MW	0.35	0.2	0.025	0.1	0.045	0.02	0.08

Fig. 7. Dust trajectories reconstructed in discharges using ICRH in addition to other auxiliary heating sources. Trajectories depicted in blue show the dust particles observed during operation of the ICR 3 antenna whose contours are highlighted in green (color online).

Fig. 8. Average spatial distribution of Single Frame Events detected at least 100 times at the same pixel location, in 74 different discharges with and without ICRH.

an additional contribution by dust produced at the antenna limiters seems reasonable, especially since the interactions between the antennas and the SOL may cause arcing, which is expected to be the main dust production mechanism in AUG [26].

Conclusions from our previous statistical analysis are however confirmed by the spatial investigation of dust distribution during ICRH, as illustrated in Fig. 7. This figure presents the dust trajectories recorded during 828 seconds of discharges in which ICRH was used in combination with other heating sources, mostly NBI (ICRH is almost never used alone in AUG). Trajectories recorded during the 85 seconds of operation of the ICR 3 antenna, which is located nearby the centre of the picture are depicted in blue. On a total of 47 dust trajectories reconstructed during ICR 3 operation, only 5 originate from the antenna or its limiters. Trajectories are also shorter by a factor of about 2 during ICRH operation, denoting a reduction of dust transport in addition to a reduction of dust rates.

The trend is similar when considering the other camera views and the other ICR antennas. Moreover, the use of ICRH has a global effect, since the reduction of dust rates is also observed when the powered ICRH antenna is not in the camera FOV. Globally, the investigation of temporal correlations between ICRH and dust occurrence shows that the average dust rate per second is 28% larger when ICRH is not operated. Furthermore, it is interesting to note that on a total of 292 shots with ICRH, 28.8% terminated with a disruption, whereas for 2096 discharges analysed without ICRH, this ratio is 40.6%. In the light of our observations, it is very likely that the lower dust rates combined with shorter dust trajectories during ICRH has a beneficial effect on plasma stability by reducing the amount of dust particles approaching the confined region. Finally, it is interesting to note that similar observations pointing out a significant reduction in dust rate during the operation of ICRH have been recently made on the EAST tokamak [28].

As a possible explanation of these results, one has to underline that ICRH is known to affect convection in the SOL [27] and the resulting modifications may influence dust motion. One has also to remember that only events tracked at least 20 frames with a total displacement of at least 5 pixels are automatically recognized by TRACE as dust fly-bys [15]. It is therefore possible that dust trajectories during ICRH are too short, or particles are not sufficiently heated by the contact with the plasma to be detected. Post-mortem analyses, which suggest that arcing
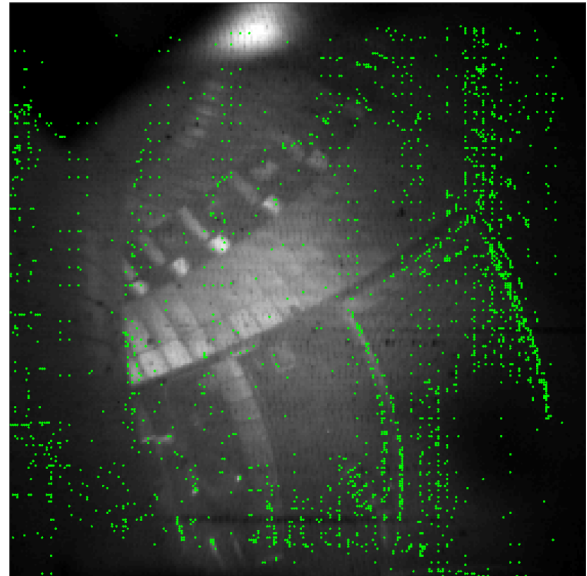
is the main process responsible of dust formation in AUG, support this idea by concluding that only a small fraction of the dust particles formed by arcs are large enough and are sufficiently heated by contact with the plasma to be visualized with fast cameras [15,26].

Videos analyzed in our study do not have sufficient spatial and temporal resolutions to discriminate arcs from noise, except in some particular cases like stationary arcs lasting 20 frames or more. Non-stationary arcs, such as unipolar arcs [29], are much more challenging to identify. Their duration is directly connected to the arc current and may vary from less than 1 microsecond to about 1 ms [30], i.e. from about 1/100 of the frame exposure time to about 10 frames. Assuming a typical duration of a few microseconds in standard AUG plasma conditions, TRACE might detect them as Single Frame Events (SFEs), therefore inseparable from noise. Unipolar arcs are known to cause numerous micro craters on metal surfaces and are likely to be promoted by ELMs and disruptions, but the mechanism causing their initiation is still insufficiently understood. However, it has been shown that they mainly arise at microprotrusions, their initiation and self-sustainment on smooth surface requiring much higher energy [30]. This suggests that unipolar arcs could repeat preferentially at some particular locations, giving the opportunity to discriminate repetitive arcs from noise.

Fig. 8 depicts the location of SFEs which are observed at least 100 times at the same pixel in a given shot, in 74 discharges under various conditions. Vertical green stripes are typical of the read noise which is due to the CMOS sensor architecture and have to be ignored. It is obvious that the residual pattern formed by SFE matches almost perfectly the contours of the ICRH antenna. Despite SFEs are certainly not all arc signatures, the fact that most of them are located at the edges of the ICRH antenna is striking. So far, our study does not establish any link between SFEs and dust. As explained before, this might be due to the fact that dust trajectories are too short or particles are not bright enough for being detected. The spatial resolution of fast cameras is only of the order of 1 centimeter with the optical setup which has been used for our analysis. In order to improve the dust detection capability, it would be worth performing measurements with higher spatiotemporal resolution in the vicinity of ICRH antennas. Meanwhile, the existing video measurements are being analyzed with the newly developed TRACK code [31] which includes major improvements compared to TRACE, opening new possibilities for the characterization of short dust trajectories.

5. Summary and outlook

Fast camera measurements recorded in 2425 discharges in the AUG tokamak have been analyzed with the aim to better understand the transport of intrinsic dust. Stereoscopic measurements supported by simulations with the DUCAD code have shown that dust motion is largely dominated by inertia for micrometric spherical W dust. It is found that only small grains of a few hundreds of nanometers in diameter or less, invisible to fast cameras, and non-spherical dust particles may experience noticeable influence of the plasma forces. The latter particles and dust grains experiencing collisions with PFCs are the only ones whose motion can significantly deviate from the inertial motion under the considered experimental conditions.

The investigation of camera measurements during VDEs confirms that upward VDEs have a stronger impact on dust activity than downward VDEs, due to larger energy release to the PFCs. The investigation of the influence of heating scenarios demonstrates that NBI increases dust rates coming from sectors where injectors are installed, while ICRH is found to significantly reduce rates and transport of dust particles in the whole plasma volume. The reduction of dust transport during ICRH is certainly an important result in the perspective of increasing the ICRH contribution to the heating of fusion plasmas in future experiments. However, in order to understand the mechanisms leading to these observations, modelling and further experimental work on dust generation and release by arcs are needed. In particular, it would be of great interest to repeat investigations on the influence of ICRH with new measurements focusing at the newly installed 3-strap ICRH antennas, which has been designed in order to reduce the impurity release.

Acknowledgements

Supplementary materials

Supplementary material associated with this article can be found, in the online version, at doi:10.1016/j.nme.2019.01.014.

References

[1] S.I. Krasheninnikov, R.D. Smirnov, D.L. Rudakov, Plasma Phys. Controlled Fusion 53 (2011) 083001.

[2] A.Y. Pigarov, S.I. Krasheninnikov, T.K. Soboleva, T.D. Rognlien, Phys. Plasmas 12 (2005) 122508.

[3] A.L. Roquemore, N. Nishino, C.H. Skinner, et al., J. Nucl. Mater. 363 (2007) 222.

[4] S.H. Hong, C. Grisolia, V. Rohde, P. Monier-Garbet, Tore Supra Team and ASDEX Upgrade Team, Nucl. Fusion 50 (2010) 035002.

[5] M. Bacharis, M. Coppins, J.E. Allen, Phys. Plasmas 17 (2010) 042505.

[6] G. De Temmerman, M. Bacharis, J. Dowling, et al., Nucl. Fusion 50 (2010) 105012.

[7] R.D. Smirnov, S.I. Krasheninnikov, A.Y. Pigarov, et al., J. Nucl. Mater. 415 (2011) S1067.

[8] K. Krieger, T. Lunt, R. Dux, et al., Journal of Nucl. Materials 415 (2011) S297.

[9] S. Ratynskaia, et al., Nucl Fusion 53 (2013) 123002.

[10] L. Vignitchouk, P. Tolias, S. Ratynskaia, Plasma Phys. Controlled Fusion 56 (9) (2014) 095005.

[11] D.L. Rudakov, A. Litnovsky, W.P. West, et al., Nucl. Fusion 49 (2009) 085002.

[12] A. Shalpegin, L. Vignitchouk, I. Erofeev, et al., Plasma Phys. Control. Fusion 57 (2015) 125017.

[13] A. Autricque, S.H. Hong, N. Fedorczak, et al., Nucl. Mater. Energy 12 (2017) 599.

[14] L. Vignitchouk, S. Ratynskaia, M. Kantor, et al., Validating heat balance models for tungsten dust in cold dense plasmas, Plasma Phys. Controlled Fusion 60 (2018) 115002https://doi.org/10.1088/1361-6587/aadbcb.

[15] F. Brochard, A. Shalpegin, S. Bardin, T. Lunt, V. Rohde, J.L. Briançon, G. Pautasso, C. Vorpahl, R. Neuand the ASDEX Upgrade Team, Nucl. Fusion 57 (2017) 036002.

[16] G. Suárez López, Modelling of dust behavior in fusion plasmas, Master Thesis report, University of Lorraine, https://hal.univ-lorraine.fr/hal-01949398, (2015).

[17] T. Lunt, J.J. Fuchs, K. Mank, Y. Feng, F. Brochard, A. Hermann, V. Rohde, N. Endstrasserand the ASDEX Upgrade Team, Nucl. Instrum. Methods Phys. Res. A 623 (2010) 812, https://doi.org/10.1016/j.nima.2010.04.150.

[18] J.E. Allen, Physica Scripta 45 (1992) 497.

[19] R.D. Smirnov, et al., Plasma Phys. Controlled Fusion 49 (2007) 347.

[20] C. Herring, M.H. Nichols, Rev. Mod. Physics 21 (1949) 185.

[21] P. Tolias, Plasma Phys. Controlled Fusion 56 (2014) 123002.

[22] M.A. Ordal, et al., Appl. Opt. 24 (1985) 4493.

[23] Y. Tanaka, R.D. Smirnov, A.Y. Pigarov, M. Rosenberg, Phys. Plasmas 15 (2008) 1.

[24] R. Marek, J. Straub, Int. J. Heat Mass Transfer 44 (2001) 39–53.

[25] A. Shalpegin, F. Brochard, S. Ratynskaia, et al., Nucl. Fusion 55 (2015) 112001.

[26] M. Balden, N. Endstrasser, P. Humrickhouse, V. Rohde, M. Rasinski, S. Lindig, R. Neuand the ASDEX Upgrade Team, Nucl. Fusion 54 (2014) 073010.

[27] V. Bobkov, M. Balden, R. Bilato, et al., Nucl. Fusion 53 (2013) 093018.

[28] S. Sarkar, R. Ding, J. Yang, H. Xie, B. Wang, J. Chen, Phys. Plasmas 25 (2018) 122505.

[29] M. Maeno, H. Ohtsuka, S. Yamamoto, et al., Nucl. Fusion 20 (1980) 1415.

[30] S. Barengolts, G. Mesyats, M. Tsventoukh, Nucl. Fusion 50 (2010) 125004.

[31] TRACK code, developed by the APREX Company: http://www.aprex-solutions.com/.